46p.

N64-24048
Code 1
CR56468
cat. 09

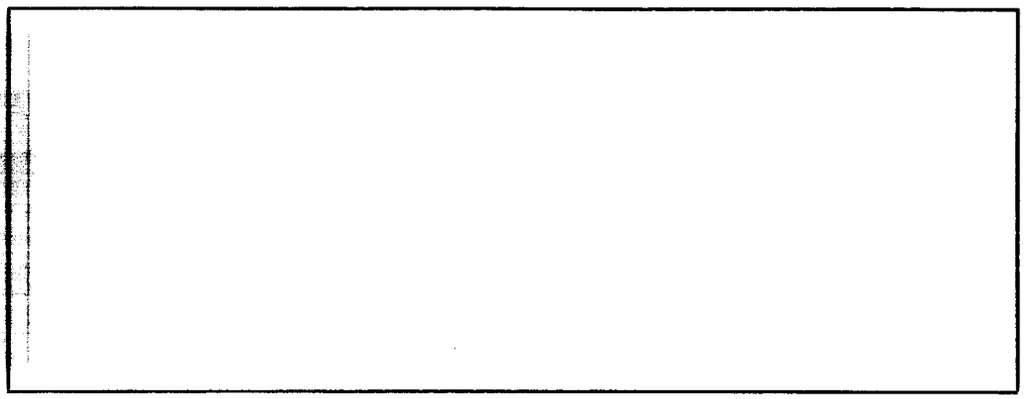

ADVANCED KINETICS

COSTA MESA CALIFORNIA

OTS PRICE

XEROX $ 4.60 ph

MICROFILM $ _____

A D V A N C E D K I N E T I C S, I N C.
1231 Victoria Street
Costa Mesa, California

"MAGNETIC FORMING COIL DESIGN AND DEVELOPMENT"

Contract NAS 8-5434

SUMMARY REPORT

Prepared for

GEORGE C. MARSHALL SPACE FLIGHT CENTER

HUNTSVILLE, ALABAMA

April 21, 1964

The following personnel has contributed to the performance of this project:

Dr. R. W. Waniek

Dr. H. P. Furth

Mr. W. D. Luedtke

Mr. R. G. Davis

Mr. D. W. Ishmael

Mr. D. R. Holt

Mr. H. J. Gilsdorf

Mr. G. N. Cirica

TABLE OF CONTENTS

LIST OF ILLUSTRATIONS

LIST OF ILLUSTRATIONS (Continued)

I) INTRODUCTION

The process of magnetic hammering against sheet metal has been studied extensively. A hammer of the type shown in Figs. 1 and 2 has been developed in the 4", 8" and 12" diameter sizes (Hammers I, II, and III). These hammers are suitable for bulging sheet aluminum alloy up to 3/4" in thickness. The hammer recoil problem has been studied, and means of recoil-absorption by clamping against the work have been developed.

The spatial distribution of the magnetic field strength, B, and its dependence on the separation, z, between hammer and work have been measured. In Fig. 3, the radial variation of B_r is graphed for various values of z, for Hammer IA. The curve "B_c" refers to the field when hammer and work are in contact ($z = 0$). The curve "B_o" is measured with the work removed ($z = \infty$). In Fig. 4, the peak values of B_r are plotted as a function of z. These graphs are for a source of 150 μf, 1 kV, 75 joules. At 10 kV, 7500 joules, the peak field B_c for $z = 0$ is 200 kilogauss. The radial dependence of B_r for $z = 0$ and ∞, is given for Hammers II and III in Fig. 7 and 8. The peak values B_c are 130 kilogauss and 85 kilogauss respectively at 7500 joules.

From Fig. 4, we see that B^2 drops off about like $.25/(.25+z)$, with z in cm. Similarly, we then expect that the resistive penetration of the field into the work and the coil surface will drop B^2 to half-value in a time, τ_r, such that the associated skin depth

$$s = 20\sqrt{\tau_r} \quad \text{cm} \tag{1}$$

is about .25 cm. Thus we see that $\tau_r \sim 150$ μsec. This time is long because of the large size of the configuration. In what follows, we are dealing with somewhat shorter forming times, and will thus ignore resistive diffusion.

II) THE THEORY OF THE FORMING OPERATION

Let us now consider the equations of motion of the metal-forming operation. There are two forces tending to resist the deformation: inertia and tensile strength. The inertial pressure is simply

$$P_i = w\rho \frac{dv}{dt} \tag{2}$$

where ρ is the mass density per unit volume and w is the sheet-metal thickness. The pressure in the z-direction due to the tensile strength is

$$P_s = S \frac{w}{R_c} \tag{3}$$

where S is the ultimate tensile strength and R_c is the radius of curvature of the sheet metal bulge being created. In terms of the displacement z of the sheet-metal, we then have

$$B^2/8\pi = P_i + P_s$$

$$= w\left(\rho \frac{d^2z}{dt^2} + S\frac{2z}{R_o^2}\right) \qquad (4)$$

where R_o is the coil radius. Strictly speaking, there must also be a term proportional to $v = dz/dt$, which represents viscosity - that is, the work dissipated frictionally in the sheet metal during forming. In the absence of such a term, Eq. 4 would say that the sheet metal springs right back after deformation! For present purposes, we simply apply Eq. 4 only during the time when $dz/dt > 0$, and consider the forming process to end there.

As will be seen in Section III, there actually is no spring-back in experiments with thin sheet metal and substantial deformation. For thick sheets and small deformations, the approximation is less good.

For convenience we introduce the "critical field" B_s[1], such that

$$\frac{B_s^2}{8\pi} = S \qquad (5)$$

For the aluminum alloys used in this experiment we have:

TABLE I

Alloy	S in 10^3 psi	B_s in Kilogauss
2219 - T37	60	330
6061 - T6	45	280
5052 - H32	33	240

Equation (4) can then be written

$$B^2/8\pi = w\left(\rho \frac{d^2 z}{dt^2} + \frac{z}{R_o^2} \frac{B_s^2}{4\pi}\right) \qquad (6)$$

Instead of using Eq. (6) directly, it is often useful to think in terms of the two conservation principles that can be derived from it: conservation of momentum and energy (per unit area, here)

$$p = \frac{1}{8\pi} \int_o^t dt\ B^2 = w\left[\rho \frac{dz}{dt} + \frac{B_s^2}{4\pi R_o^2} \int_o^t dt\, z\right] \qquad (7)$$

$$E = \frac{1}{8\pi} \int_o^t dt \left(\frac{dz}{dt}\right) B^2 = w\left[\frac{1}{2} \rho \left(\frac{dz}{dt}\right)^2 + \frac{B_s^2 z^2}{8\pi R_o^2}\right] \qquad (8)$$

From Eqs. (7) and (8) we can draw several important practical conclusions. Let the forming process consist of a time τ_f during which a field $\overline{B}$ is acting, followed by a time τ_i, during which the field is off and the sheet metal coasts to a stop, as in Fig. 9. Let the displacement at the end of time τ_f be D_1 so that from Eq. (8)

$$E_1 = \frac{\overline{B^2}}{8\pi} D_1 \tag{9}$$

At $t = \tau_f$ then, we have approximately,

$$D_1 \frac{\overline{B^2}}{8\pi} \approx w \left(2\rho \frac{D_1^2}{\tau_f^2} + \frac{B_s^2 D_1^2}{8\pi R_o^2}\right) \tag{10}$$

so that

$$\overline{B^2} = w\left(\frac{16\pi\rho D_1}{\tau_f^2} + \frac{B_s^2 D_1}{R_o^2}\right) \tag{11}$$

Defining

$$\overline{B}_o = \frac{\sqrt{w D_1}}{R_o} B_s \tag{12}$$

and

$$\tau_{fo} = \frac{4R_o\sqrt{\pi\rho}}{B_s} \tag{13}$$

we can write Eq. (11) as

$$\overline{B^2} = \overline{B_o^2}\left(1 + \frac{\tau_{fo}^2}{\tau_f^2}\right) \qquad (14)$$

Secondly, we have at time $t = \tau_f + \tau_i$, that is, at the end of the forming process:

$$E_1 = D_1 \frac{\overline{B^2}}{8\pi} = \frac{wD^2}{8\pi R_o^2} B_s^2 \qquad (15)$$

where $z = D$ is the total displacement at the end of the process. Thus, we see that

$$\frac{D^2}{D_1^2} = \frac{\overline{B^2}}{\overline{B_o^2}} = 1 + \frac{\tau_{fo}^2}{\tau_f^2} \qquad (16)$$

which is another way of writing Eq. (14). From (15) we have also

$$\overline{B} = \frac{\sqrt{wD}}{R_o} \sqrt[4]{1 + \frac{\tau_{fo}^2}{\tau_f^2}}\, B_s \qquad (17)$$

It is of incidental interest to find the "coasting time" τ_i, during which the sheet metal moves from $z = D_1$ to $z = D$, while its kinetic energy is converted to work. From Eq. (8) we find

$$2\rho \frac{(D - D_1)^2}{\tau_i^2} \approx \frac{B_s^2 (D^2 - D_1^2)}{8\pi R_o^2} \qquad (18)$$

during the coasting phase, so that

$$\tau_i = \tau_{fo} \left(\frac{D - D_1}{D + D_1}\right)^{1/2} \qquad (18a)$$

For Hammer I, τ_{fo} is typically 200 μsec.

Equation (17) shows that the total deformation achieved is not extremely sensitive to the duration of the field pulse, but that a lower applied field $\bar{B}$ is required if τ_f/τ_{fo} is large. Let us define Case I, when $\tau_f >> \tau_{fo}$ and Case II, when $\tau_f << \tau_{fo}$. In Case II, the field strength $\bar{B}$ needed to achieve a given deformation D is greater by a factor $(\tau_{fo}/\tau_{f\,II})^{1/2}$.

Whether Case I or II is preferable in a given situation, depends on a number of practical considerations. For example, which case is energetically more efficient depends on what fraction of the magnetic energy input is left in the hammer after the forming operation. Ideally, the change in hammer inductance due to the displacement of the sheet metal is desired to be very large, and Case II then offers twice as high an efficiency, approaching 100%. In the present experiments, however, the ideal situation is far from being realized. The approximation of constant hammer inductance during forming is more nearly applicable, especially for deformations of less than .25 cm (cf. Fig. 5). In that case, the energetic efficiency for Case I is simply greater by the factor $\overline{B^2}/\overline{B_o^2}$, where $\bar{B}$ refers to the field needed in Case II.

Another practical consideration enters, however; namely, that of hammer recoil for a given total deformation D. For given D, the input energy E_1 is fixed. From Eqs. (7) and (8), we have

$$p_1 = \frac{\bar{B}^2}{8\pi} \tau_f \tag{19}$$

$$E_1 = \frac{\bar{B}^2}{8\pi} \tau_f \left\langle \frac{dz}{dt} \right\rangle \tag{20}$$

We see that p_1 varies inversely with the mean velocity $\langle dz/dt \rangle$ that is reached by the sheet metal during the time τ_f. Obviously, a higher $\langle dz/dt \rangle$ is reached in Case II, and thus the recoil momentum is lower. Specifically, we have

$$\left\langle \frac{dz}{dt} \right\rangle = \frac{D_1}{\tau_f} = \frac{D}{\sqrt{\tau_f^2 + \tau_{fo}^2}} \tag{21}$$

The recoil momentum is then

$$p_1 = \frac{E_1}{\left\langle \frac{dz}{dt} \right\rangle} = \frac{wD}{8\pi R_o^2} B_s^2 \sqrt{\tau_f^2 + \tau_{fo}^2} \tag{22}$$

Evidently p_1 is greater by a factor τ_{fo}/τ_{f1} in Case I than it is in Case II. The minimum recoil momentum, as obtained in Case II, is

$$p_{min} = \frac{wD}{8\pi R_o^2} B_s^2 \tau_{fo} = \frac{wD B_s \sqrt{\rho}}{4R_o \sqrt{\pi}} \tag{23}$$

The recoil velocity U of the hammer is given by

$$MU = \pi R_o^2 p_1 \tag{24}$$

where M is the mass of the hammer. Thus, we have

$$U = \frac{wD}{8M} B_s^2 \sqrt{\tau_f^2 + \tau_{fo}^2} \tag{25}$$

and

$$U_{min} = \frac{wDR_o B_s \sqrt{\pi\sigma}}{4M} \tag{26}$$

TABLE II

Hammer	M Mass Kilograms	Umin Min. Recoil Velocity cm/sec
I	8.4	140 wD
II	25.7	92 wD
III	38.6	92 wD

The parameters of the hammers studied are summarized in Table III.

TABLE III

HAMMER:	IA	IB	IC	II	III
Radius R_o (cm)	5	5	5	10	15
Turns	5.7	10	10	6.7	6.5
Weight (Kg)	8.4	8.4	8.4	25.7	38.6
Coil Thickness (cm)	2.5	1.3	2.5	3.8	5
Inductance L_o (μh)	.37	3.4	2.3	1.1	1.6
Inductance in Contact with Work L_c (μh)	.17	1.1	.77	.39	.56
For 150 μf (.15 μh Source)					
1/4-cycle τ_r^o (μs)	13	36	30	22	25
1/4-cycle in Contact with Work τ_r^c (μs)	10	22	18	14	16
At 10kV (7500 Joules)					
Peak Field B_o (kG)	60	70	70	30	25
Peak Field in Contact with Work B_c (kG)	200	260	200	130	85
Peak Current I_o (Ka)	170	65	75	105	90
Peak Current in Contact with Work I_c (Ka)	220	105	125	160	140
Input Energy E_m^o (Kj)	5.3	7.3	7.0	6.5	6.7
Input Energy in Contact with Work E_m^c (Kj)	4.1	6.5	6.2	5.2	5.7

III) METAL-FORMING STUDIES

The hammers have been tested on various thicknesses of several types of aluminum alloy sheet. The results are in good agreement with the theory developed in the last section.

Figures 10 - 13 illustrate how the forming process takes place as a function of time. To obtain these results, a laminar light beam and a photomultiplier were used. A cylindrical die was slit along its length with a width of .020" in the direction of the expanding boundary. Diametrically opposite to this slit, a number of minute collimating holes were drilled directed at the slit itself. Behind these holes a conical light collector was placed adjacent and contoured to the cyclindrical wall and the light signal was properly piped out through a 1 foot long light pipe to a 931 photomultiplier. The shielded tube was far enough from the magnet so that no noise pickup due to the discharge was registered down to the lowest sensitivity levels used (5 mV/cm). A stable dc light source was located in front of the 20 mil slit with an appropriate diffuser so as to establish an even distribution of the light flux. The expanding metallic boundary is darkened with an extremely thin layer of black lacquer paint. Under static conditions the photomultiplier detects a dc level corresponding to the light flux penetrating through the slit and collected through the multiplicity of holes into the light pipe system. When a boundary is deformed

under the action of the transient magnetic pressure, the light level decreases because a progressively larger portion of the slit is darkened by the moving boundary. Assuming complete proportionality between the darkened area of the slit and the linear expansion (this was checked separately by means of progressively blackening the slit with tape) the output signal detected corresponds to the location of the boundary as a function of time. This method worked out very well, and on a dual beam oscilloscope we could display the photometric trace and the magnetic field trace at the same time. From these oscillograms we could compute the instantaneous speed of the expanding boundary by differentiation of the curves at a number of points on the oscillogram (the oscillogram gives a representation of distance as a function of time). The resultant velocities and the accelerations obtained (the accelerations were similarly derived graphically by double differentiation of the distance versus time curve) are presented in Figs. 10 - 13. It is interesting to notice that in general the acceleration remains positive as long as a field is present. After this phase, the deformed sheet is coasting at constant speed and thereafter the deceleration starts setting in.

The characteristic times τ_{fo} are calculated from Eq. (13), for Hammer I:

5052 - H32 $\quad \tau_{fo} = 240$ μsec

6061 - T6 $\quad \tau_{fo} = 210$ μsec

The effective acceleration time τ_f is approximately 120 μsec. Thus, we may use Eq. (16) and (18a) to calculate D/D_1 and τ_i, and compare the results with Figs. 10 - 13.

TABLE IV

Alloy	Calculated		Observed	
	$\frac{D}{D_1}$	τ_i μsec	$\frac{D}{D_1}$	τ_i μsec
5052 - H32	2.2	150	2	220
6061 - T6	2.0	120	2	200

The main discrepancy is that the sheet metal does not slow down as sharply as one might expect at the end of the process. It looks as though the effective tensile strength is dropping there.

It remains to compare the observed and predicted values of D for given $\overline{B}$. Now, B is varying strongly through the time τ_f, due to oscillation ($\overline{B^2} = \frac{1}{2} B^2_{max}$), damping (1/e in 70 μsec), and the z-dependence effect illustrated in Fig. 4. Using Eq. (8), to make a numerical integration over B^2, we find $\overline{B}^2 D_1 \approx 2 \cdot 10^9$ gauss^2 cm for the case of Fig. 10 at 7 kV. From Eq. (15), we then obtain D = 3 cm, which is about right. For Fig. 12, D is

somewhat smaller, since B_s is larger.

The dependence of D on $\bar{B}$, B_s and w is seen more directly in Figs. 14 - 18. We can check the observed proportionalities against Eq. (15), provided we take into account the drop-off of $\bar{B}$ with increasing D (as in Fig. 4). Using

$$B^2 \sim B_c^2 \left(\frac{.25}{.25 + z}\right)$$

in Eq. (8), and using $D \sim 2D_1$, which is the case for all the present data, we have roughly

$$D \propto \frac{R_o B_c}{\sqrt{w}\, B_s} \sqrt{\log_e (.5 + D) - \log_e (.5)} \qquad (27)$$

where D is in cm. The quantity $Q = D/\sqrt{\log_e (.5 + D) - \log_e (.5)}$ is tabulated below.

TABLE V

Q	D
0	0
.60	.5
.95	1
1.6	2
2.2	3
2.8	4
3.2	5

In Fig. 19 all the data of Figs. 14 - 16 have been plotted in terms of Q vs $R_o B_c/B_s\sqrt{w}$. Ideally one would expect a single straight line from Eq. (27), but the fit is only approximate.

As is clear from Fig. 17, Hammer 1B achieves substantially greater deformation than Hammer I for the same energy input. If one plots deformation vs B_c, however, as in Fig. 18, there is only some 10 - 20% more deformation for Hammer 1B. This result agrees with Eq. (17), which says that D is not sensitive to τ_f.

IV) HAMMER RECOIL PROBLEMS

Recoil data were obtained by coupling a low mass, low friction linear transducer to the hammer coil itself. The data obtained on maximum linear recoil and maximum recoil speed as a function of input energy are given in Figs. 20 - 22. It is interesting to notice in this context that the coil starts moving only approximately 200 μsec after field maximum. This time corresponds to the duration of the traversal of a sound wave moving at typical velocities of 600 m/sec through about 10 cm of the reinforced plastic material (insulation in the shell interior).

These measurements involve recoil from a massive, motionless plate, so that we must apply Eqs. (19) and (24) directly, instead of using Eq. (25),

where the hammer recoils during an actual forming operation.

Again, we have to estimate $\overline{B^2}$. This time we have $z \approx 0$ during the field-pulse, so we need merely consider the factor of about 1/6 introduced by ringing and decay during τ_f. Using

$$U = \frac{R_o^2 \overline{B^2} \tau_f}{8M} \tag{28}$$

with $\overline{B^2} = \frac{1}{6} B_c^2$, we calculate the following recoil velocities.

TABLE VI

Hammer	τ_f μsec	Energy Kilojoules	U cm/sec Calculated	U cm/sec Observed
I	60	3	60	55
II	90	7.5	120	120
III	100	7.5	90	90

Note that τ_f is short here, since there is no forming, so that the coil inductance is minimal.

The values of U calculated from Eq. (25), using typical w and D at the indicated energy levels, yield somewhat smaller recoil velocities than

those observed here, as one would expect.

Fig. 23 compares the recoil velocity for Hammers 1A and 1B at the same values of B_c. It is clear that the recoil of Hammer 1B is substantially greater, just as one would expect from Eq. (19), since τ_f is longer for Hammer 1B.

V) APPLICATION TO THE CORRECTIVE REALIGNMENT OPERATION ON SATURN

Having derived the basic equations of the forming and recoil processes, and having checked them against experiment, we now can draw conclusions about the Saturn magnetic hammering operations. The object here is to displace 3/4" sheets of 2219 - T37 alloy by typical distances in the .01 - .1 inch range.

Since D is so small, we can neglect the effect shown in Fig. 4, and we need simply allow for oscillation and decay, letting $\overline{B^2}$ be about $B_c^2/6$ during the time τ_f. Using Eq. (17) we can calculate the following approximate values of $\overline{B}$ for D = .2 cm.

TABLE VII

Hammer	τ_f μsec	τ_{fo} μsec	$\bar{B}$ kG	B_c kG
I	60	180	73	180
II	90	360	42	105
III	100	540	32	80

The above numbers would indicate that 7.5 kilojoules is just adequate for the job, but because of spring-back and similar effects encountered in the small-displacement limit, it will be best to allow for another factor of 2 in energy, and have a 15 kilojoule capability.

It will also be noted that the characteristic times τ_{fo} are extremely long - much longer than initially estimated in the present research program. This situation makes for slightly higher $\bar{B}$ requirement (see Eq. 17) than is strictly necessary. The initial motivation in keeping τ_f short was to minimize recoil momentum, but from Eq. (25) we see that U is not very sensitive to τ_f when $\tau_f^2 \ll \tau_{fo}^2$, which is the case in Table VII. Thus, it is perhaps desirable to increase τ_f. This aim, however, can be accomplished only to a limited extent by reducing the ringing frequency - i.e., by increasing the number of turns in the hammer coils. Hammer IB has twice as many turns as Hammer IA,

and oscillates twice as slowly, but the decay time of the field is only slightly longer, and this is the effective time τ_f. The point here is that the diffusion time τ_r of Eq. (1) is what really limits the effective time τ_f, no matter how many turns a coil has.

The real advantage in going from Hammer IA to Hammer IB is in avoiding loss of energy in the internal impedance of the capacitor bank (see Table III). The moral of the story is that enough turns shoule be put into the hammer coil so that efficient operation is achieved with the given capacitor bank. Hammer IA is almost as effective as Hammer IB, when a really fast capacitor bank is used. If such banks are not available, Hammer IB is preferable. Fortunately, Hammers II and III have sufficiently high inductances so that the problem is not acute in those cases.

The recoil velocities reached in the Saturn operation are of the order 100 cm/sec (see Table II). For recoil distances of a few cm, shock-absorption times of order 50 millisec are encountered. For Hammer III this means a deceleration force of about 100 Kg. This force is readily supplied by a shock-absorber based on suction cups (see Fig. 21), as provided to the GCMSFC by Advanced Kinetics, Inc.

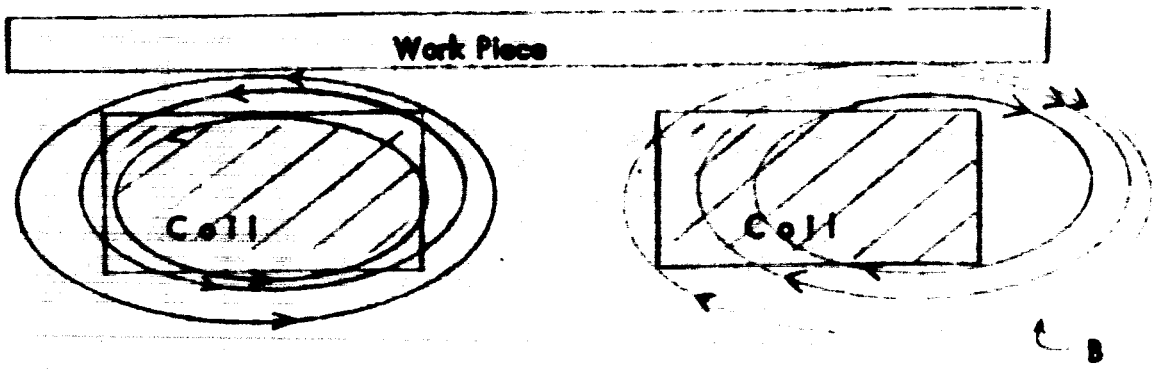

Fig. 1: Schematic of Hammer Coil and Work Sheet

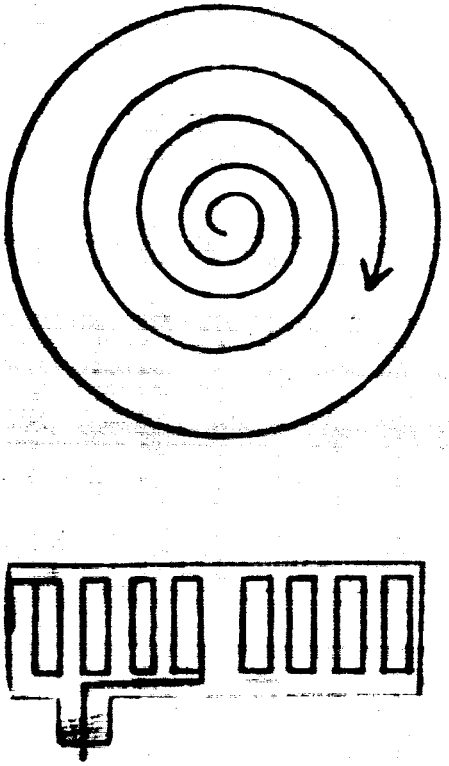

Fig. 2: Schematic of Typical Hammer Coil

Fig. 3: Radial Variation of B_r as a Function of Work Sheet Position (Hammer IA)

C_B = 150 μf

E_B = 1.0 kV

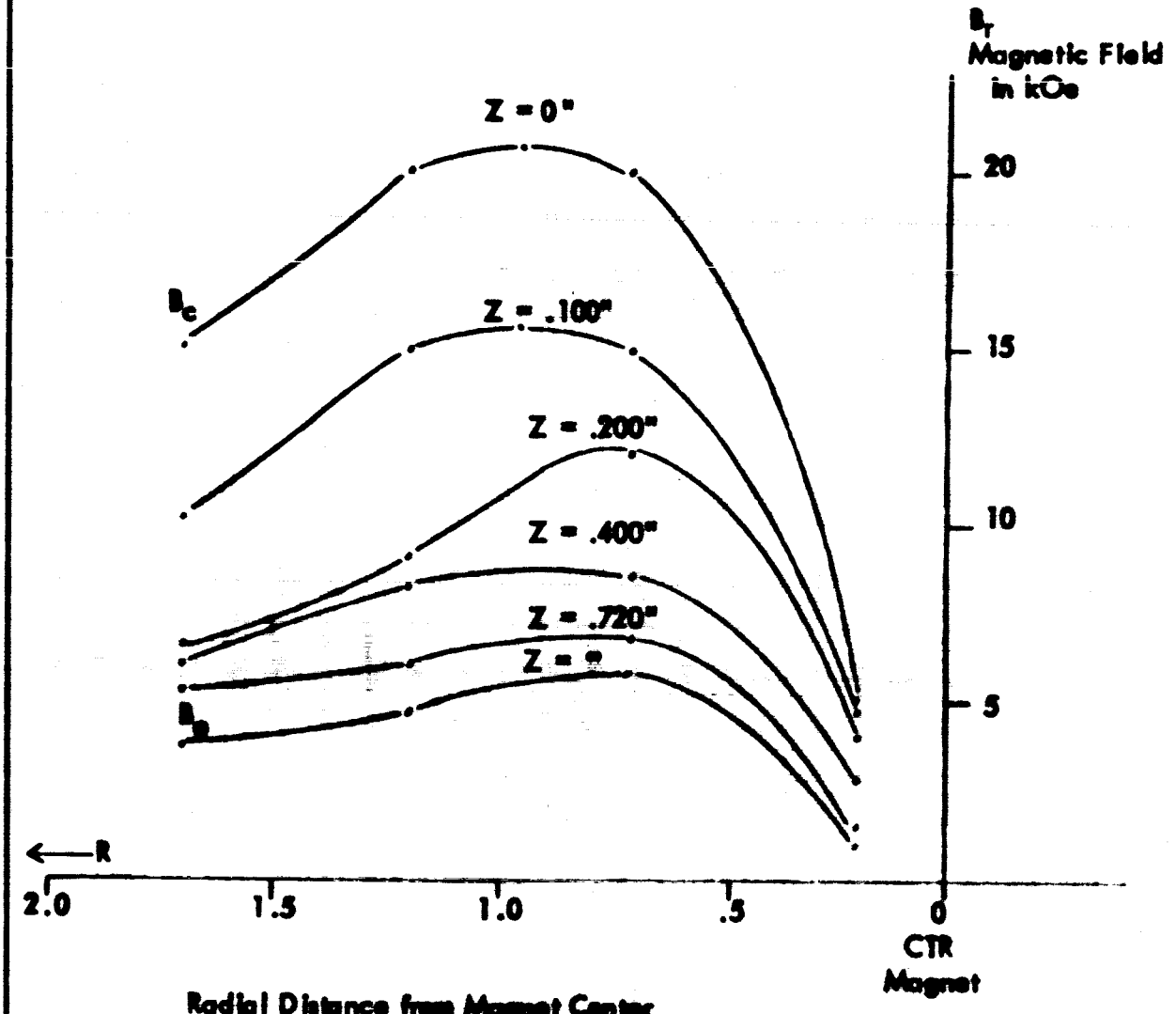

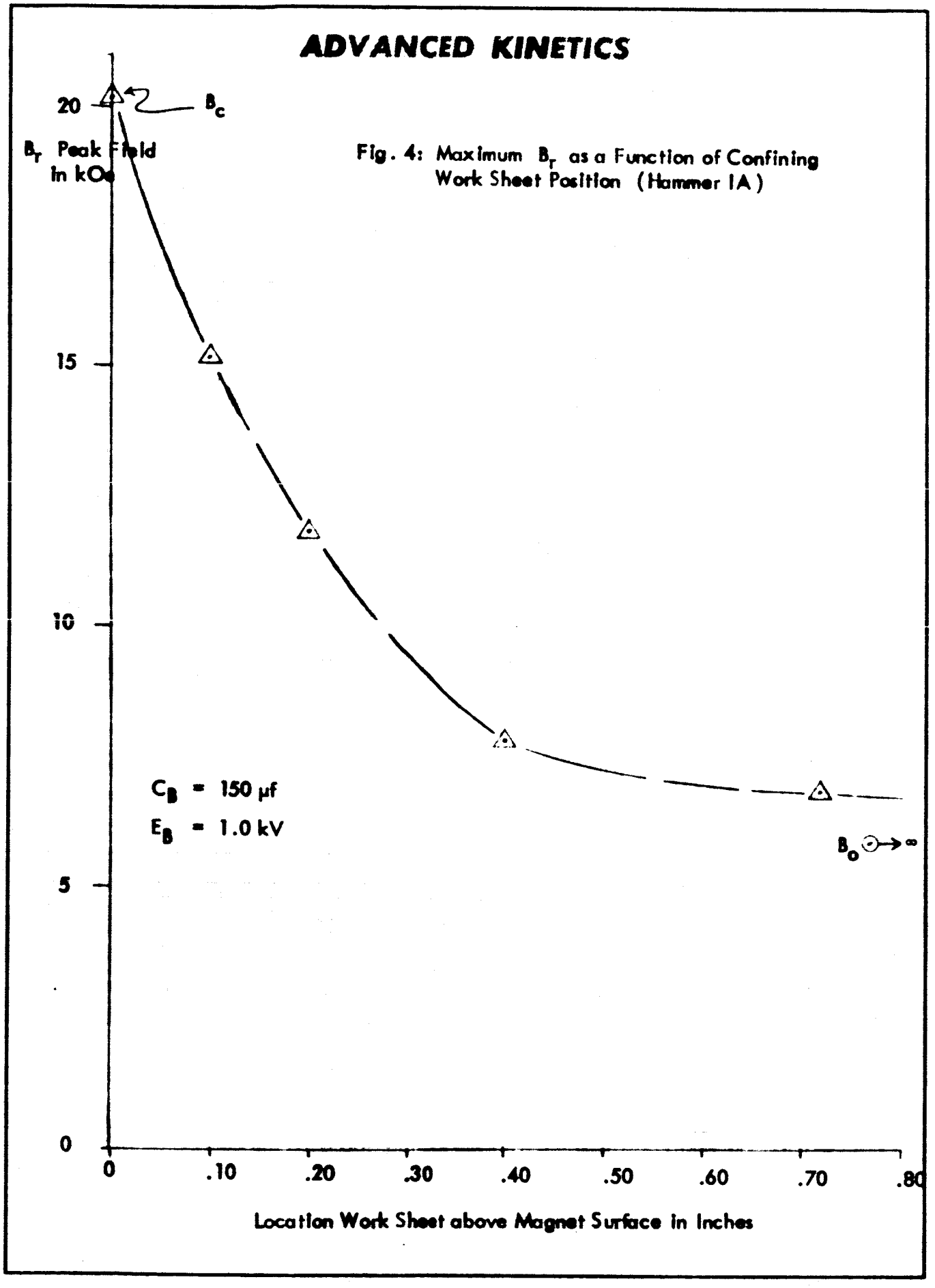
ADVANCED KINETICS
Fig. 4: Maximum B_r as a Function of Confining Work Sheet Position (Hammer 1A)
B_r Peak Field in kOe
20
15
10
5
0
B_c
C_B = 150 μf
E_B = 1.0 kV
B_o
0
.10
.20
.30
.40
.50
.60
.70
.80
Location Work Sheet above Magnet Surface in Inches

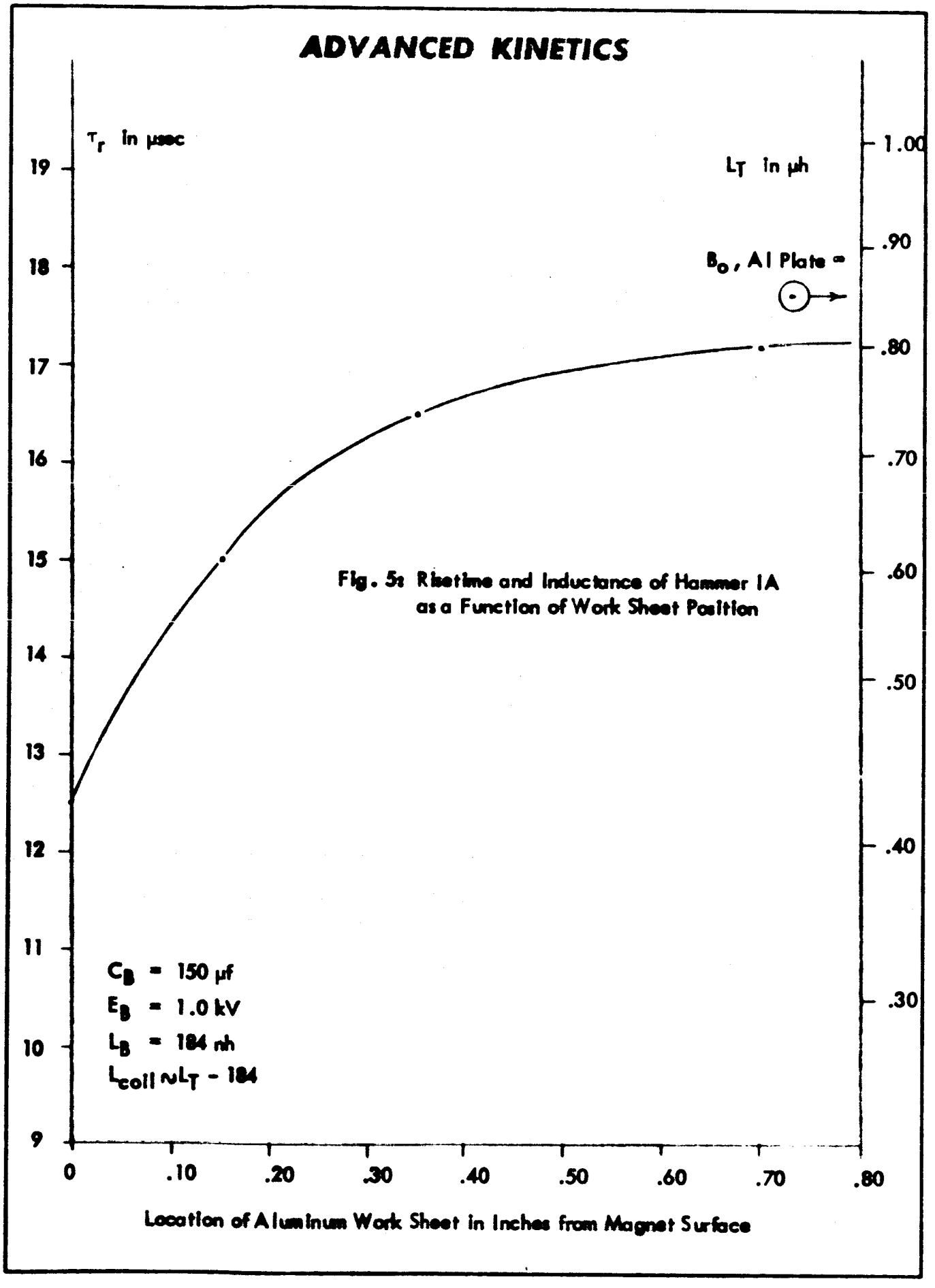

Fig. 5: Risetime and Inductance of Hammer 1A as a Function of Work Sheet Position

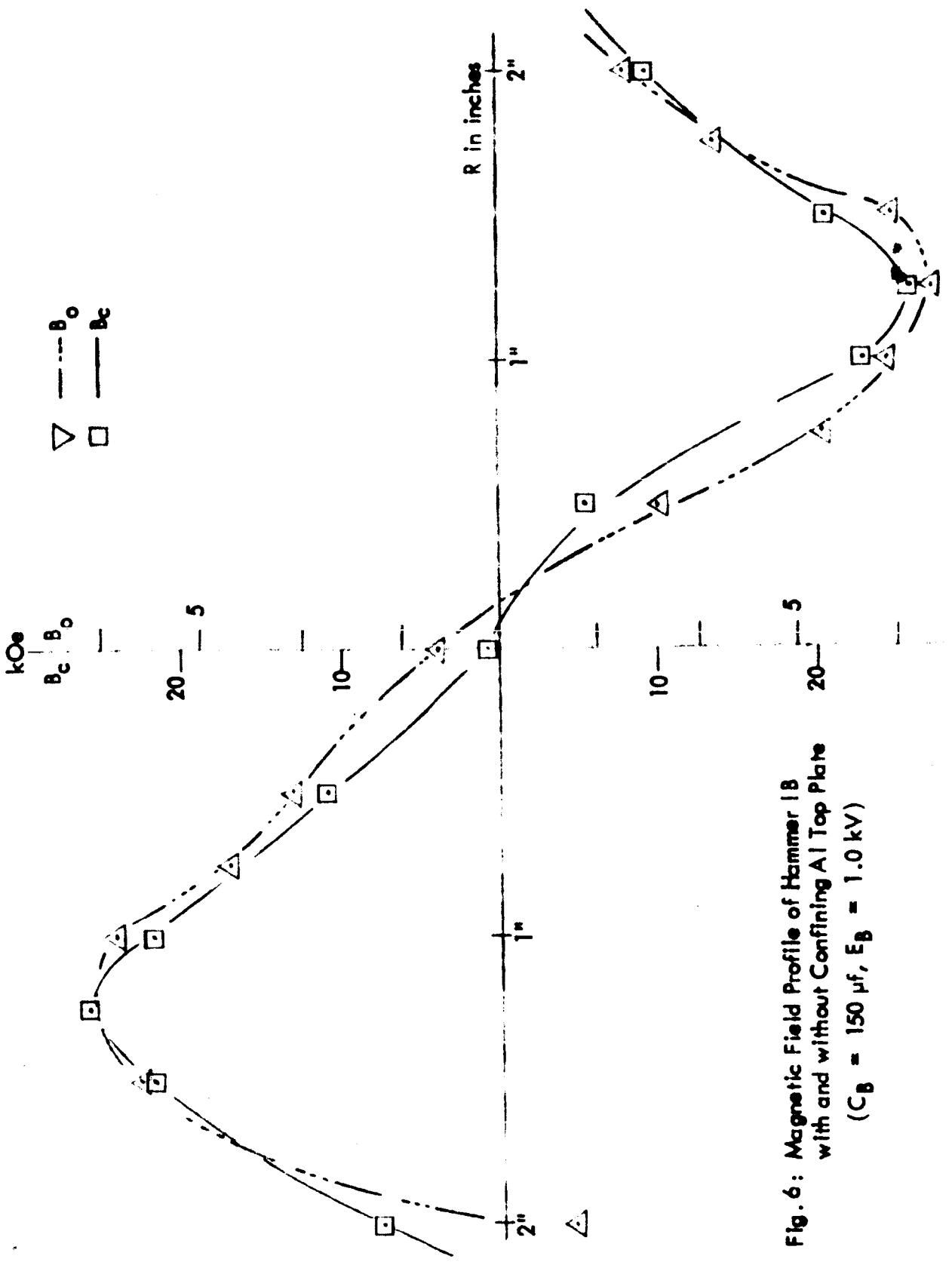

Fig. 6: Magnetic Field Profile of Hammer 18 with and without Confining Al Top Plate (C_B = 150 μf, E_B = 1.0 kV)

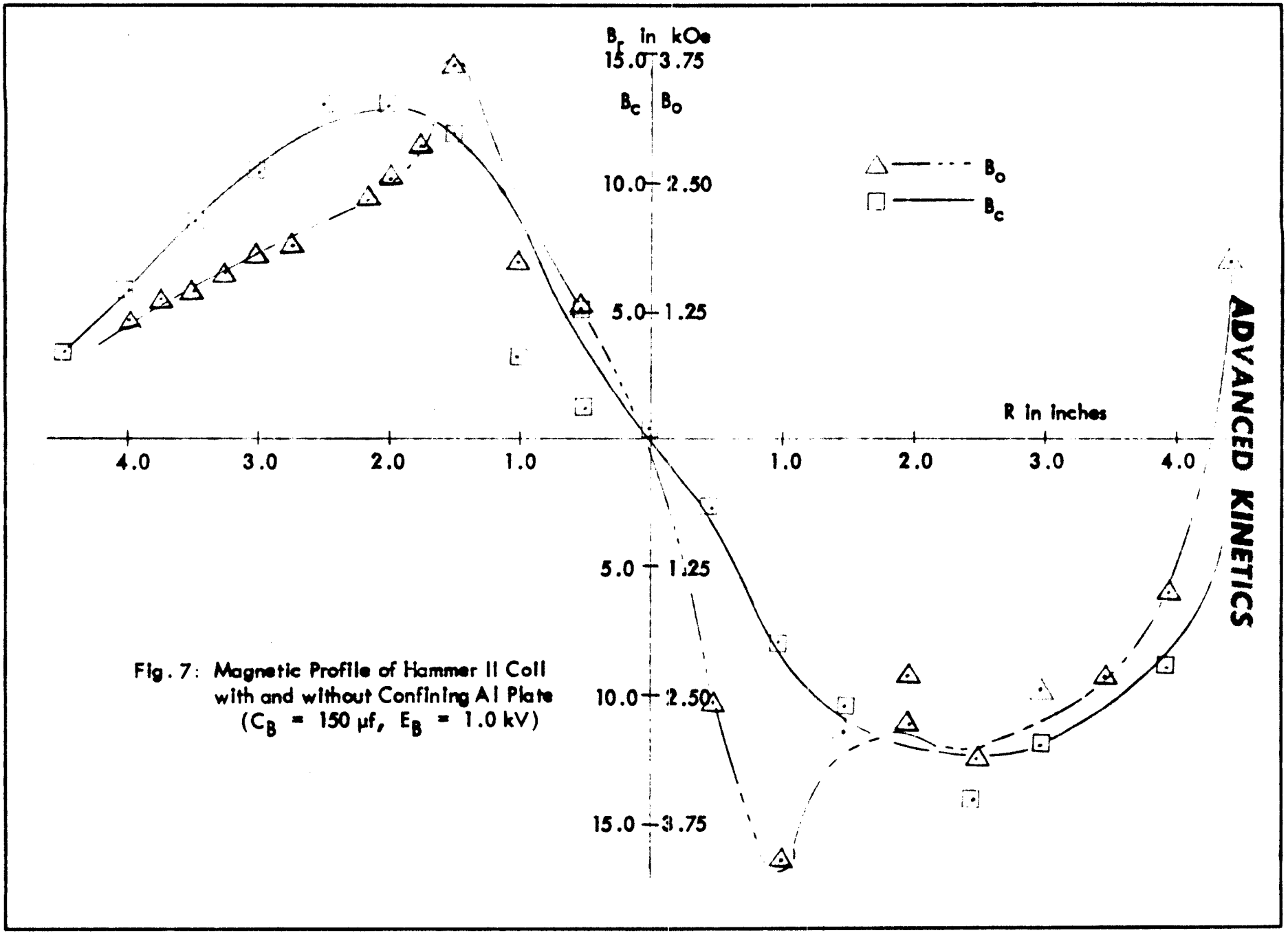

Fig. 7: Magnetic Profile of Hammer II Coil with and without Confining Al Plate (C_B = 150 μf, E_B = 1.0 kV)

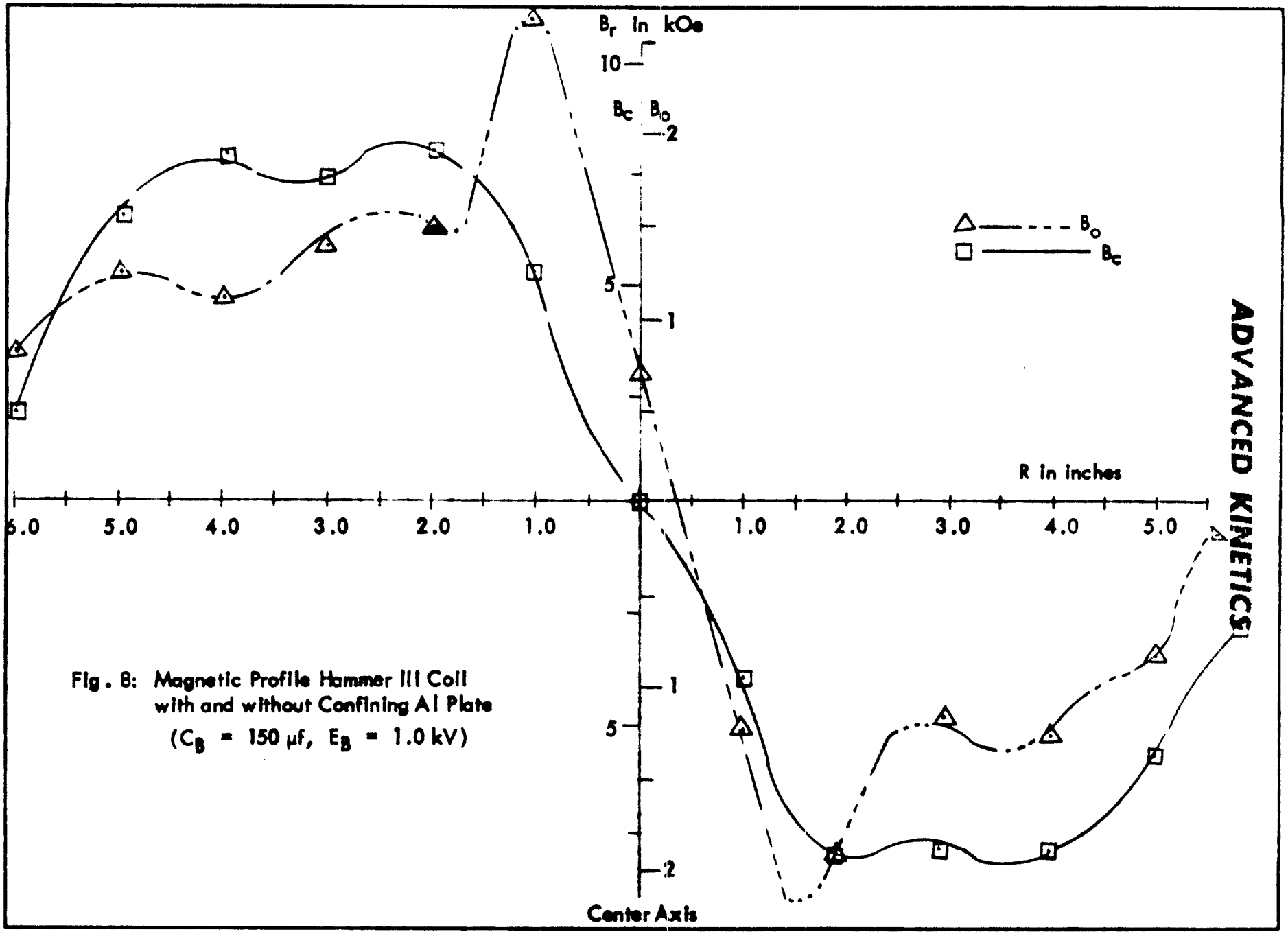

Fig. 8: Magnetic Profile Hammer III Coil with and without Confining Al Plate (C_B = 150 μf, E_B = 1.0 kV)

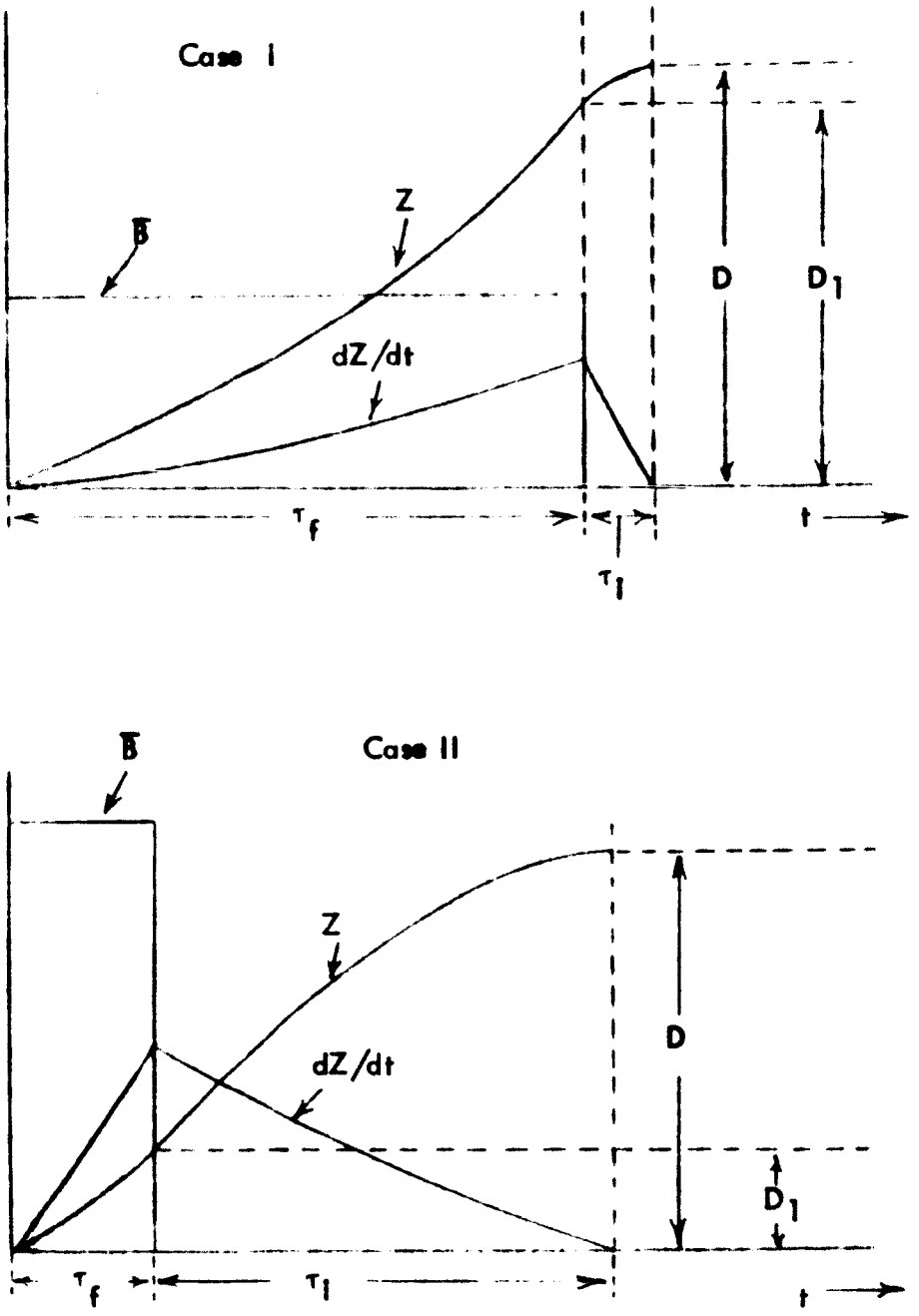

Fig. 9 Ideal Parametric Time Diagram

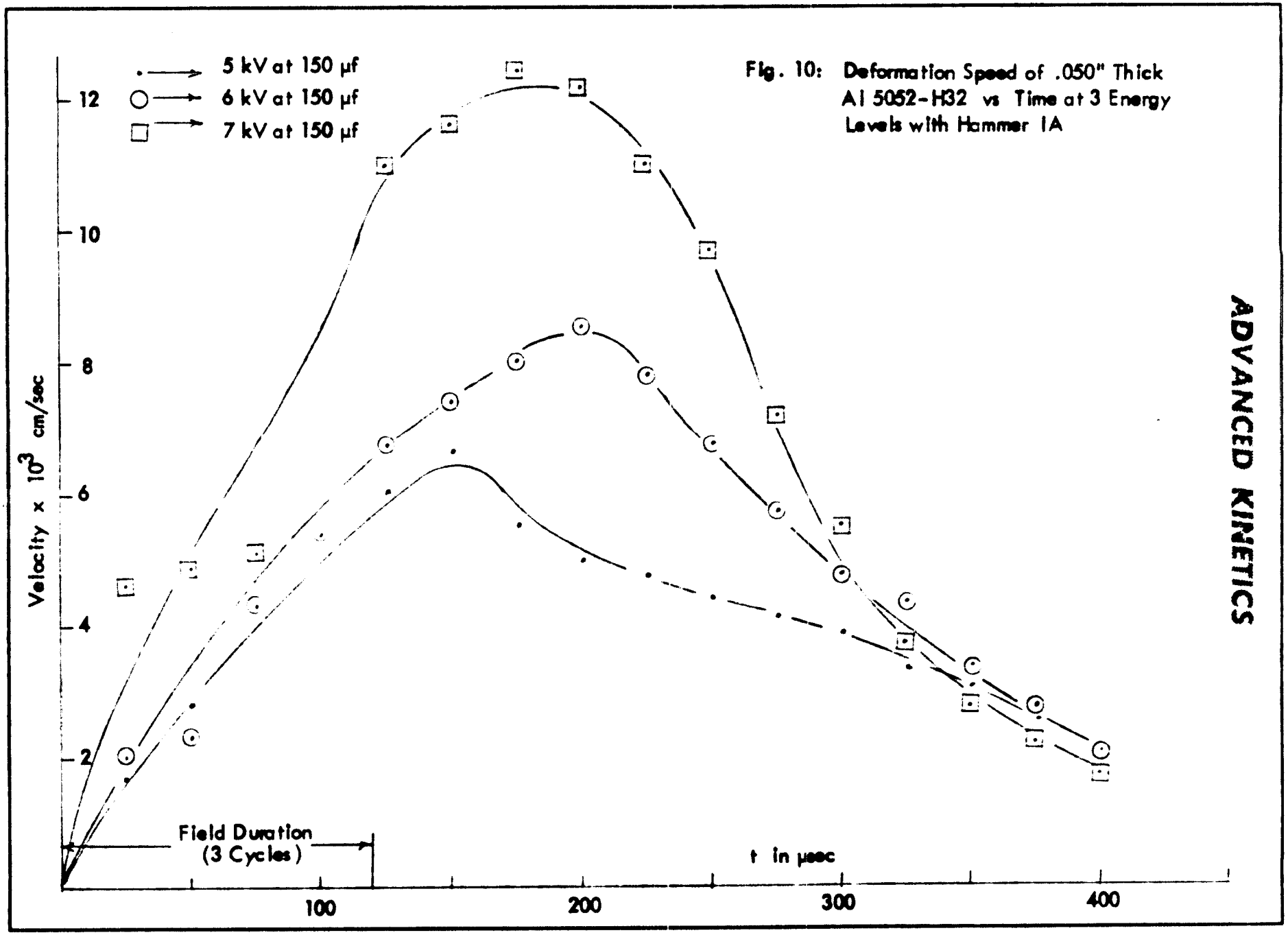

Fig. 10: Deformation Speed of .050" Thick Al 5052-H32 vs Time at 3 Energy Levels with Hammer 1A

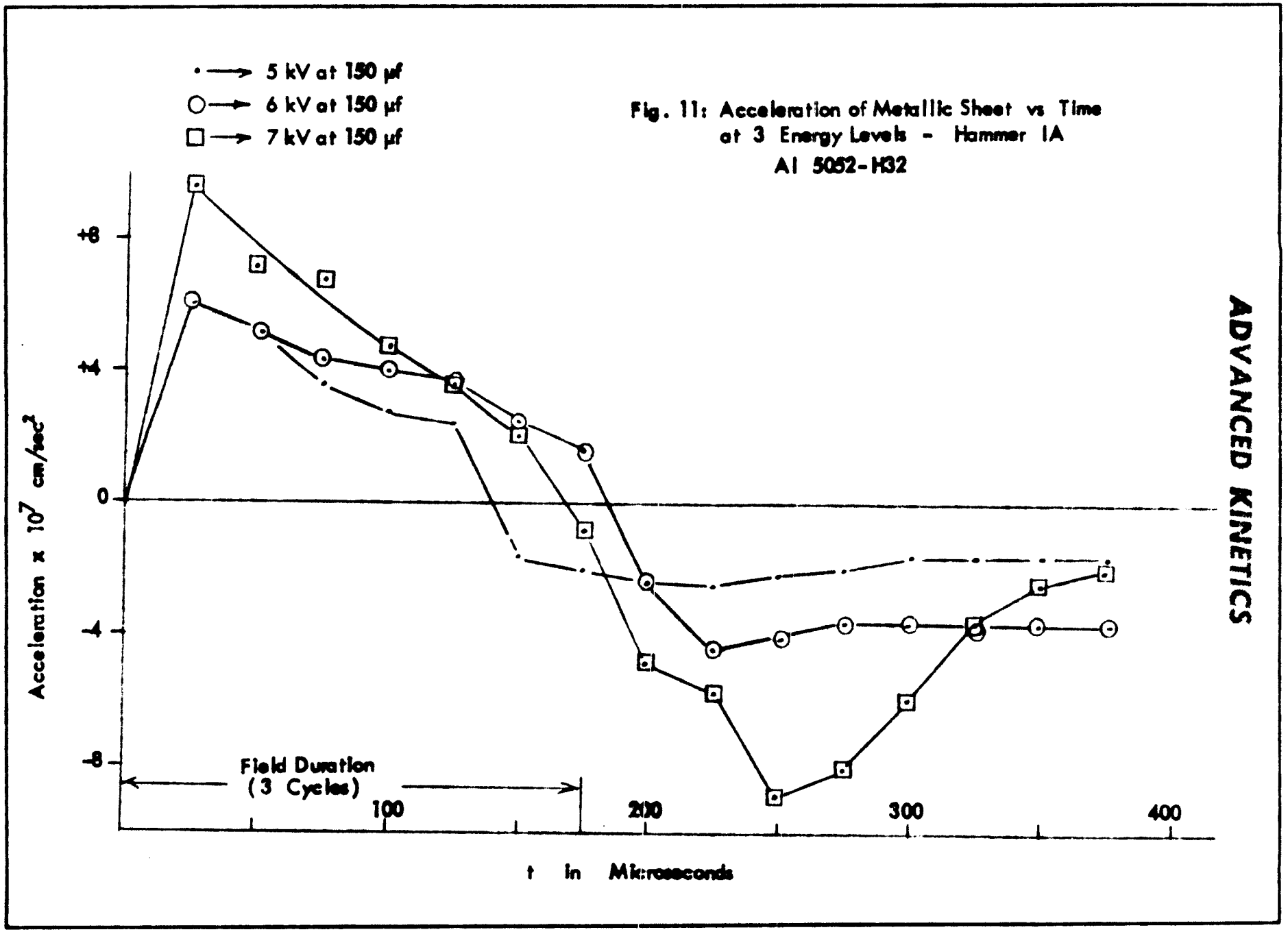
5 kV at 150 μf
6 kV at 150 μf
7 kV at 150 μf
Fig. 11: Acceleration of Metallic Sheet vs Time at 3 Energy Levels - Hammer IA
Al 5052-H32
+8
+4
0
-4
-8
Acceleration x 10^7 cm/sec^2
Field Duration (3 Cycles)
100
200
300
400
t in Microseconds
ADVANCED KINETICS

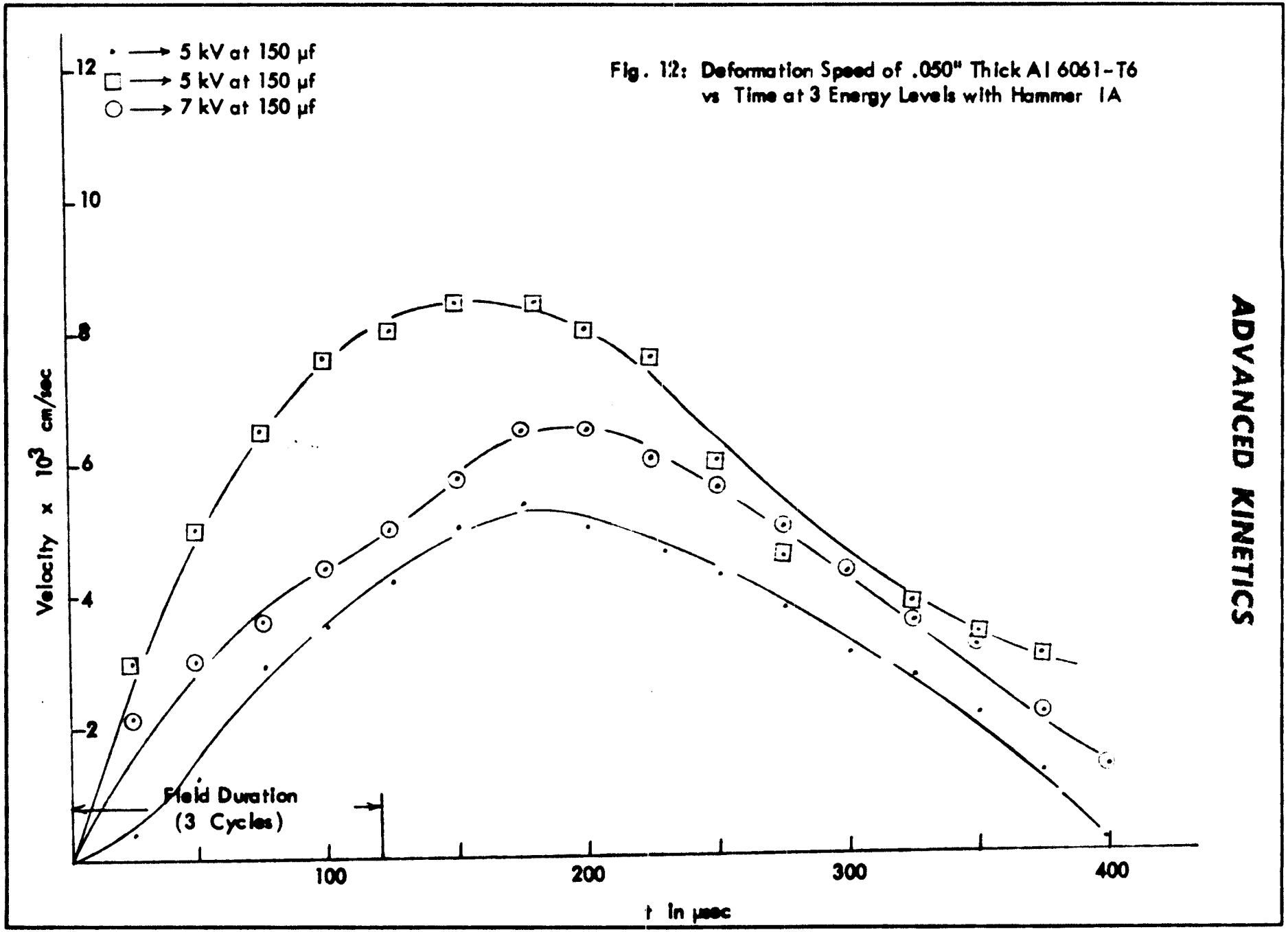
• ⟶ 5 kV at 150 μf
□ ⟶ 5 kV at 150 μf
○ ⟶ 7 kV at 150 μf
Fig. 12: Deformation Speed of .050" Thick Al 6061-T6 vs Time at 3 Energy Levels with Hammer 1A
Velocity x 10³ cm/sec
12
10
8
6
4
2
Field Duration (3 Cycles)
100
200
300
400
t In μsec
ADVANCED KINETICS

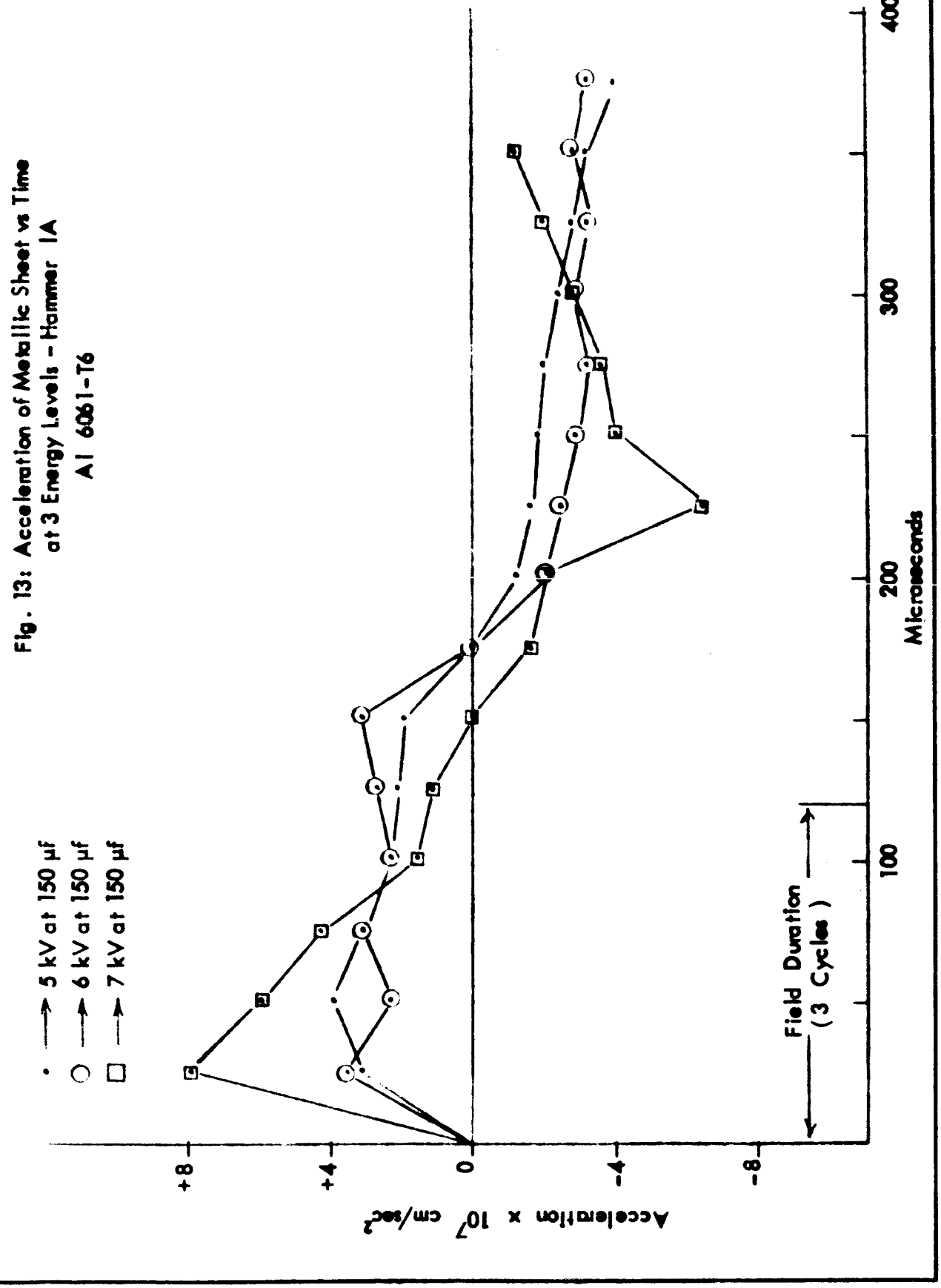

Fig. 13: Acceleration of Metallic Sheet vs Time
at 3 Energy Levels - Hammer 1A
Al 6061-T6

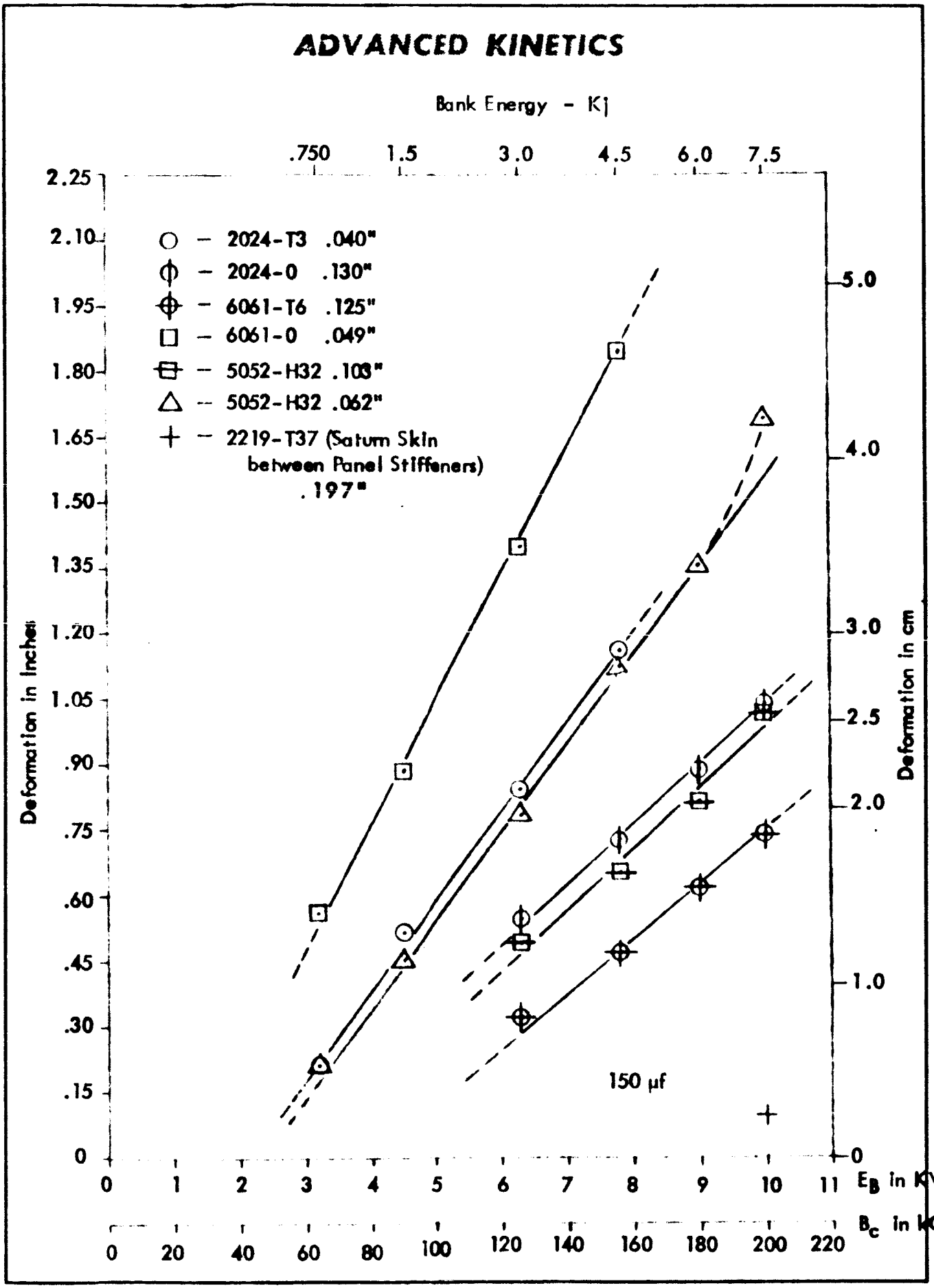

Fig. 14: Deformation vs Energy Data with Hammer IA Coil

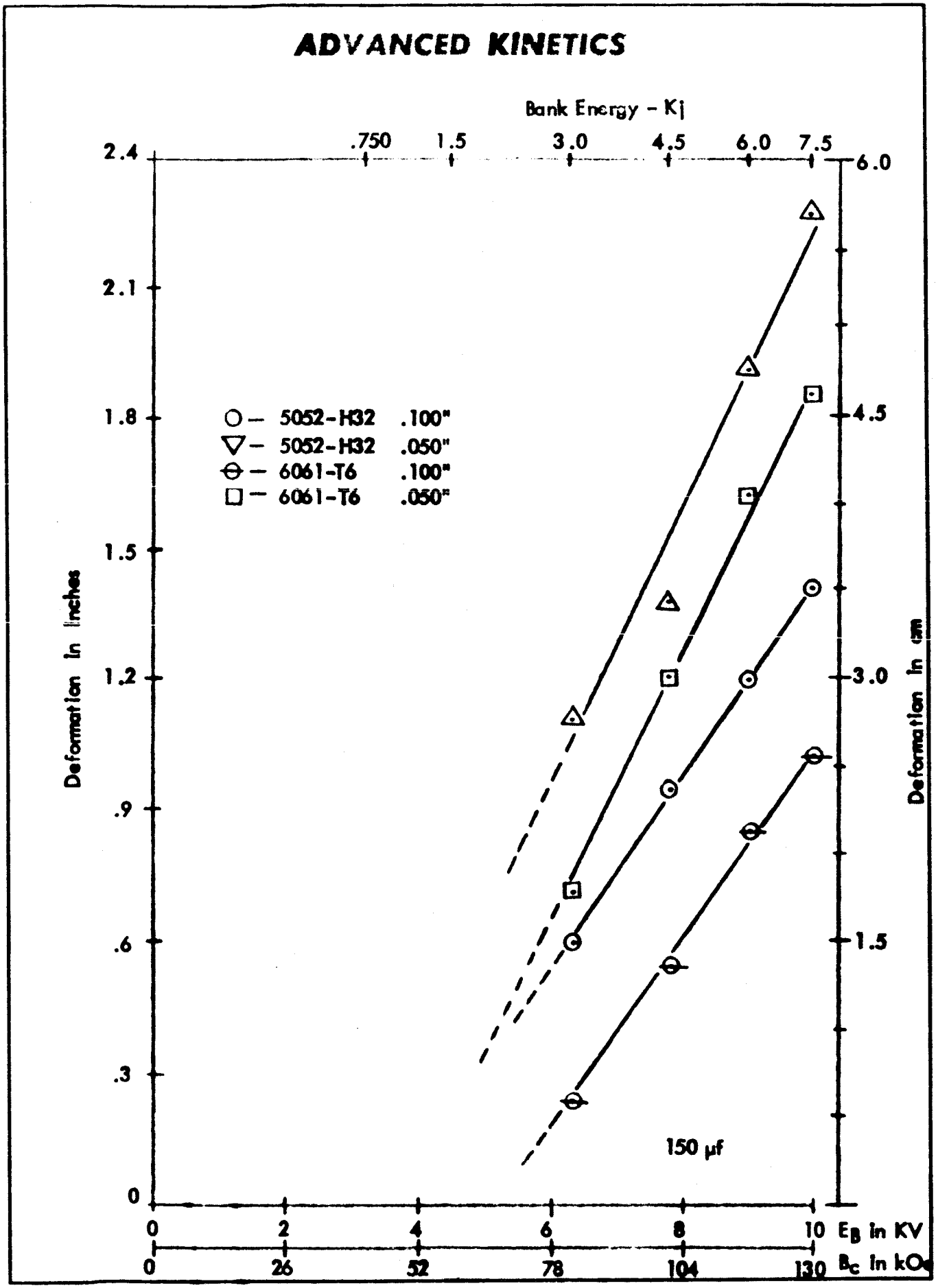

Fig. 15: Deformation vs Energy Data with Hammer II Coil

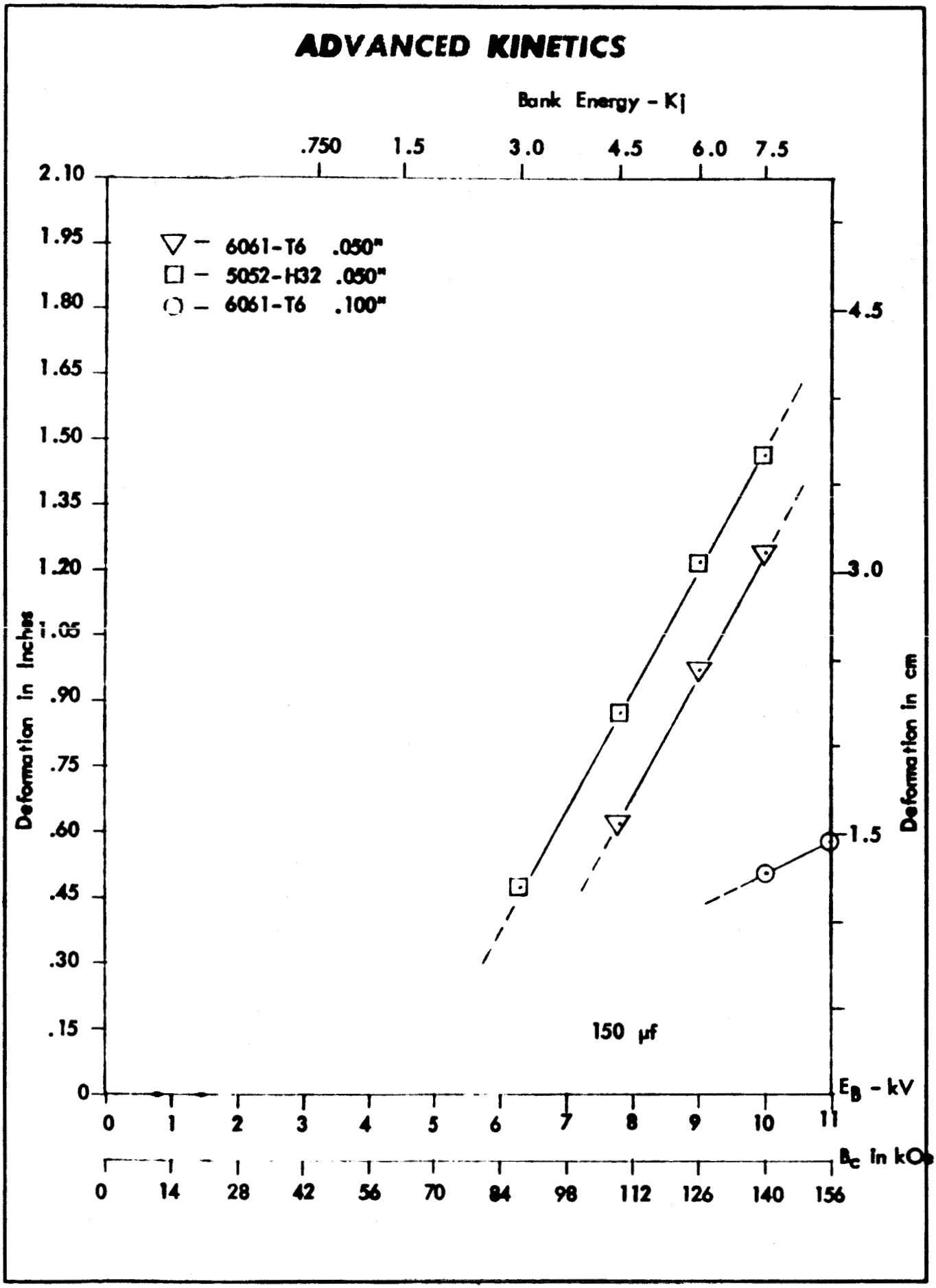

Fig. 16: Linear Deformation vs Energy for Hammer III Coil

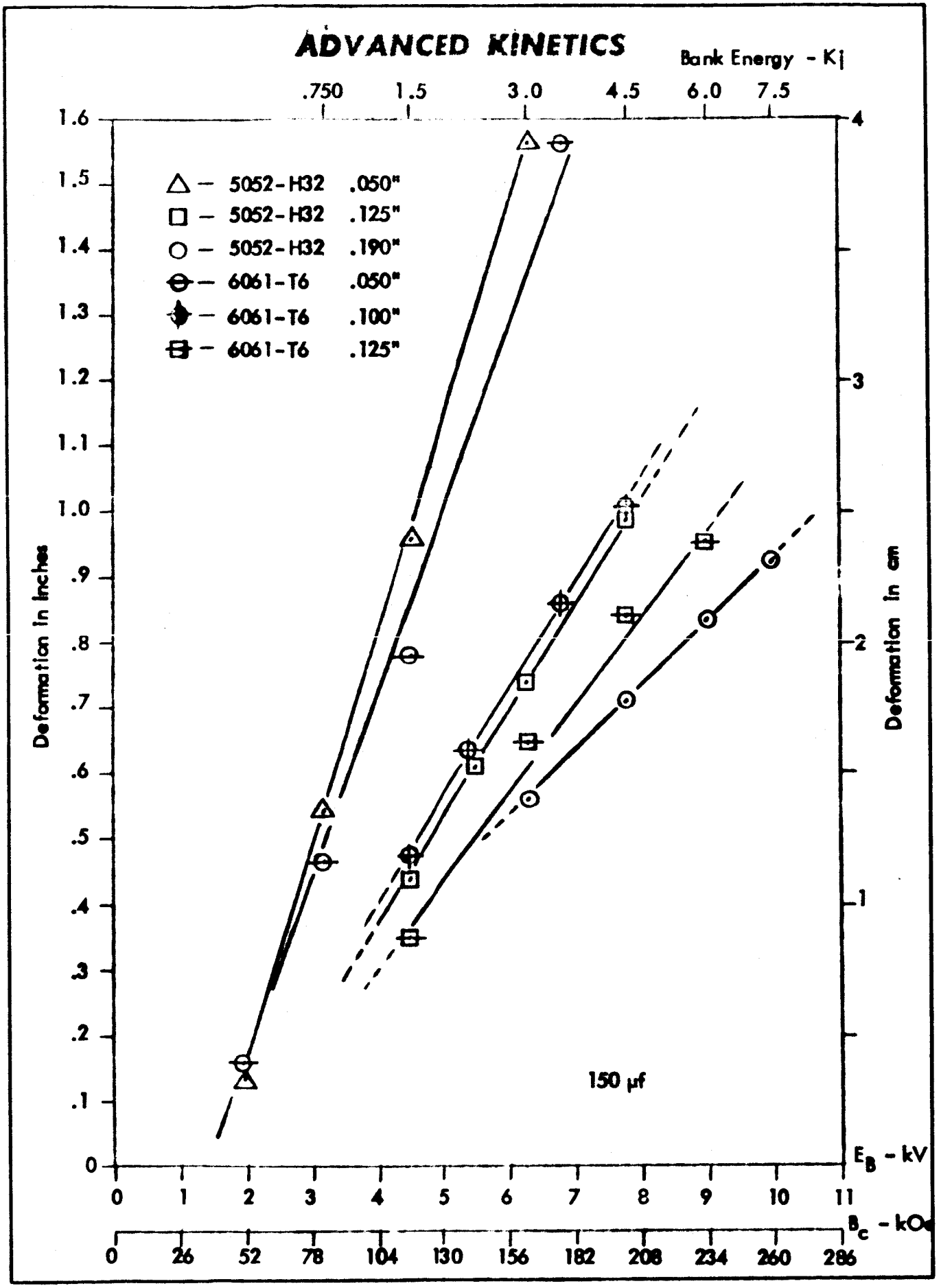

Fig. 17: Linear Deformation vs Energy for Hammer 1B Coil

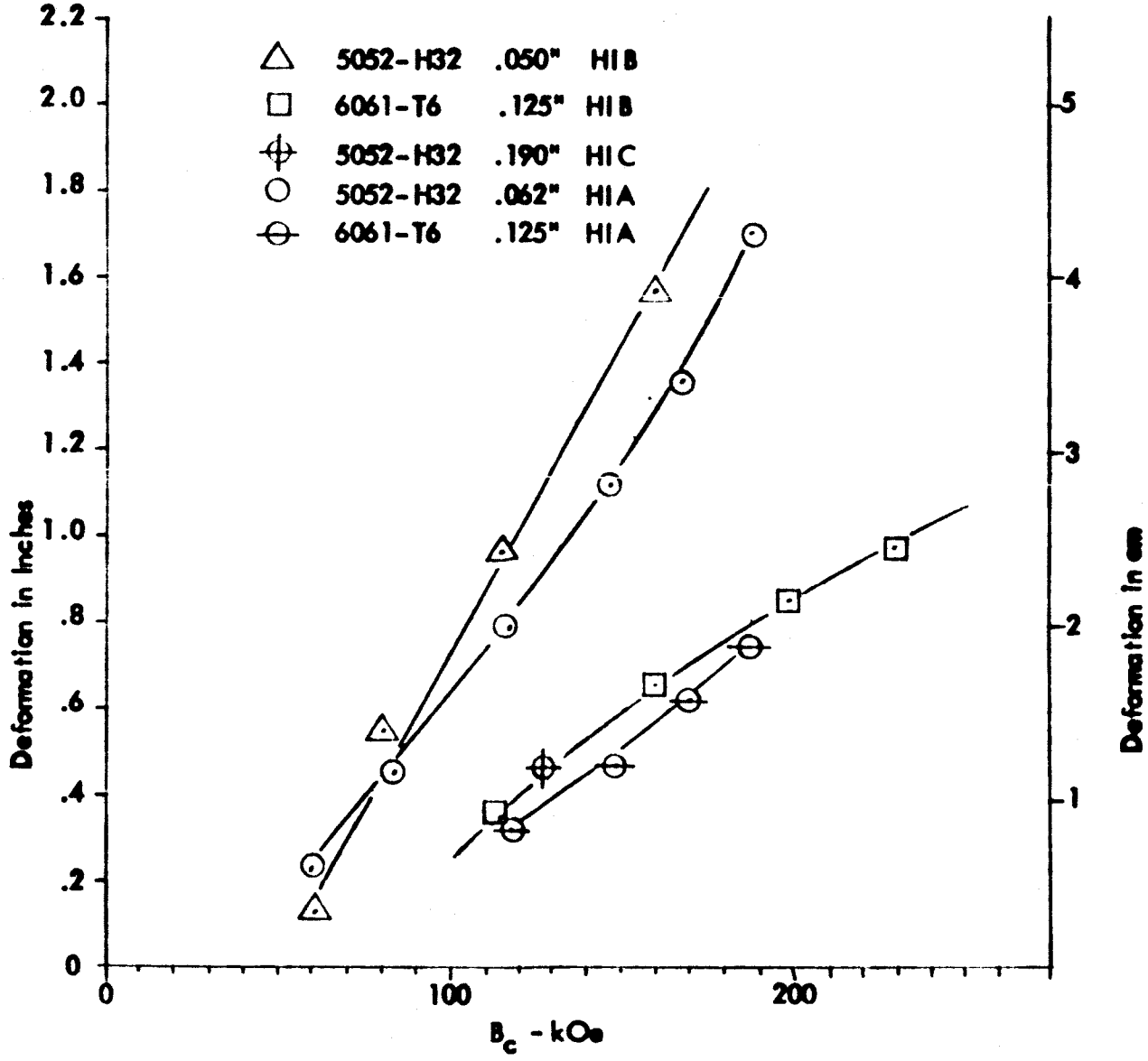

Fig. 18: Comparison of Linear Deformation vs Field for H IA, H IB, and H IC.

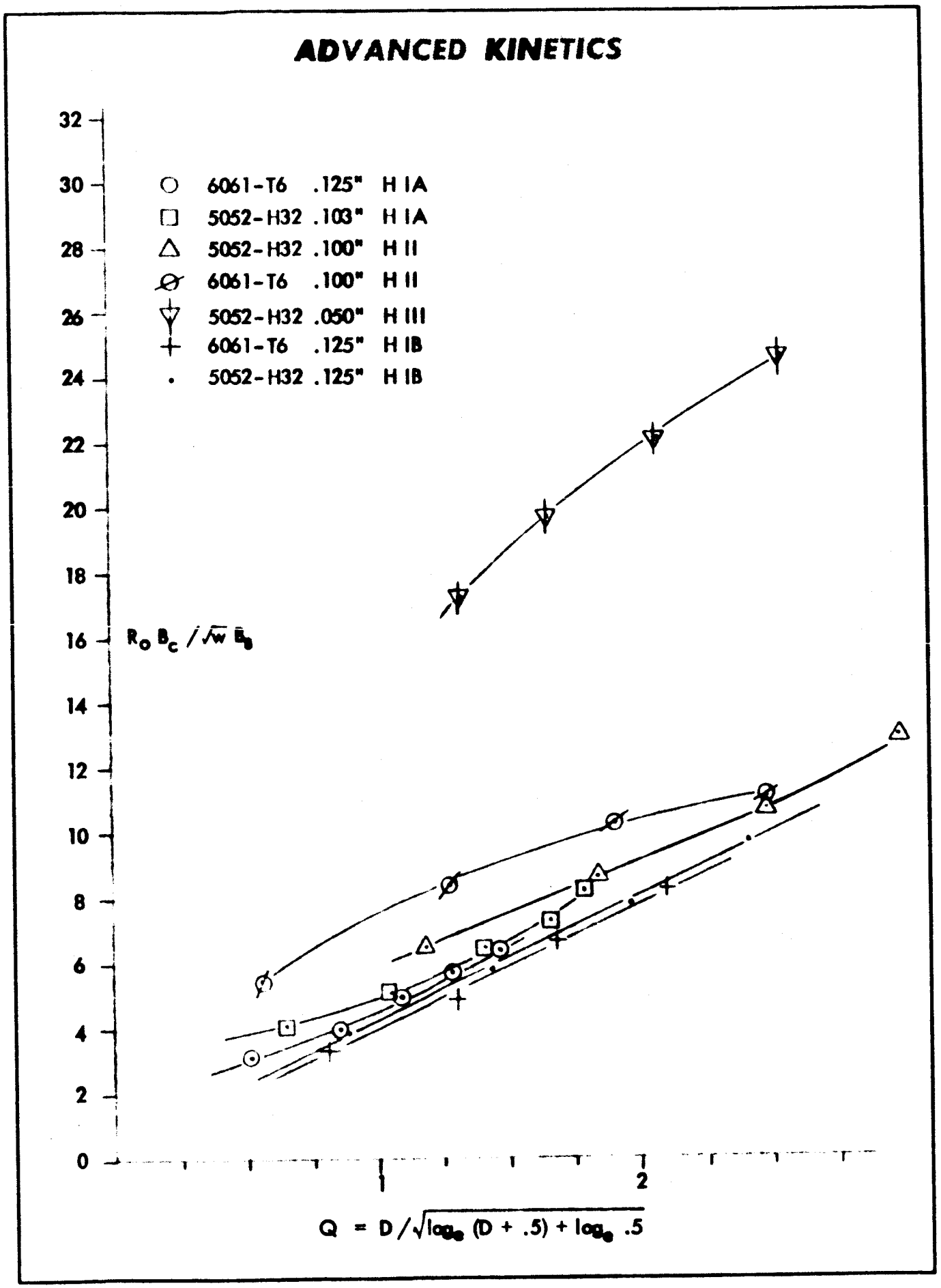

Fig. 19: Graphical Analysis of H IA, H IB, H II, and H III

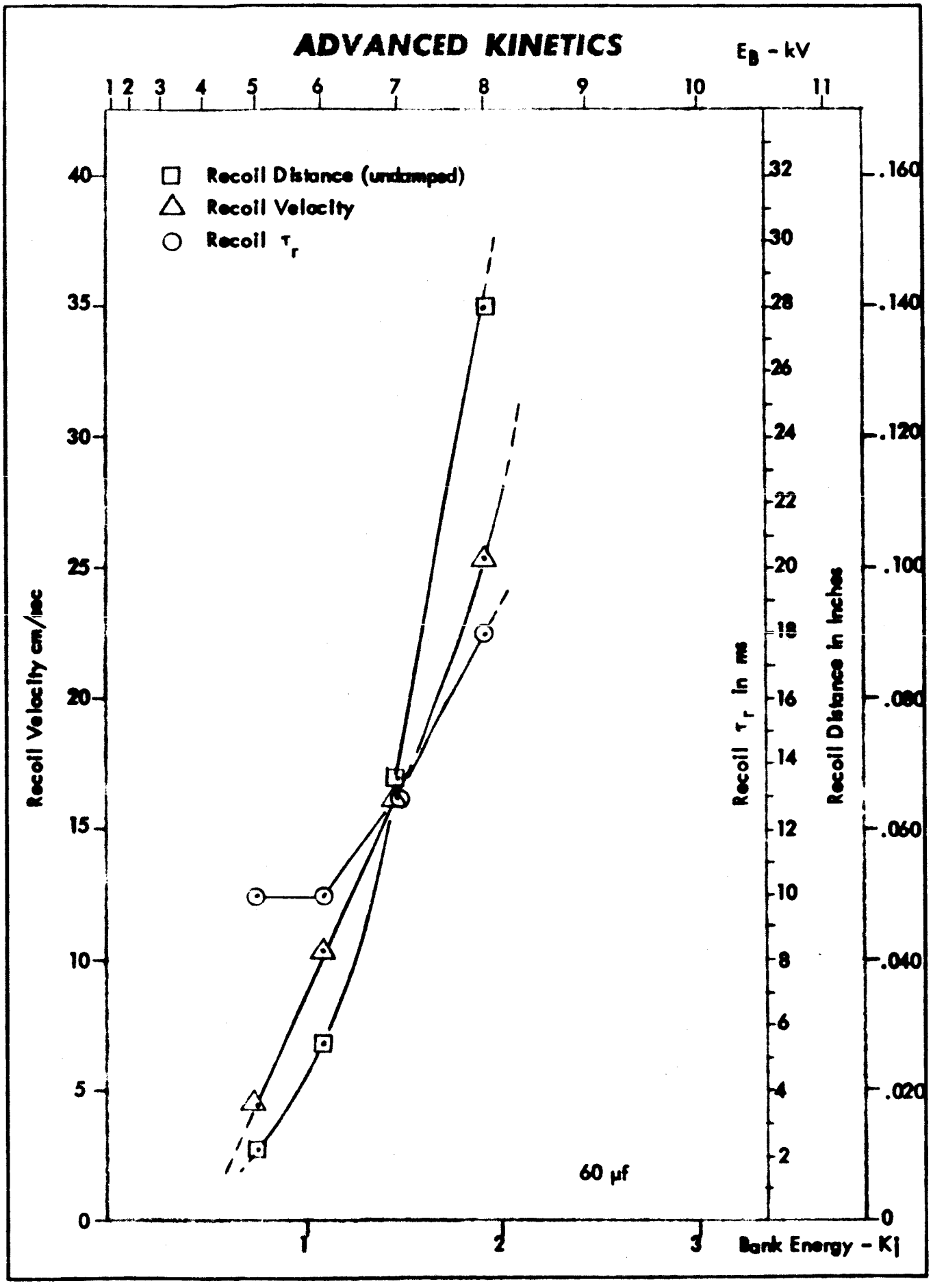

Fig. 20: Recoil Data for Hammer IA

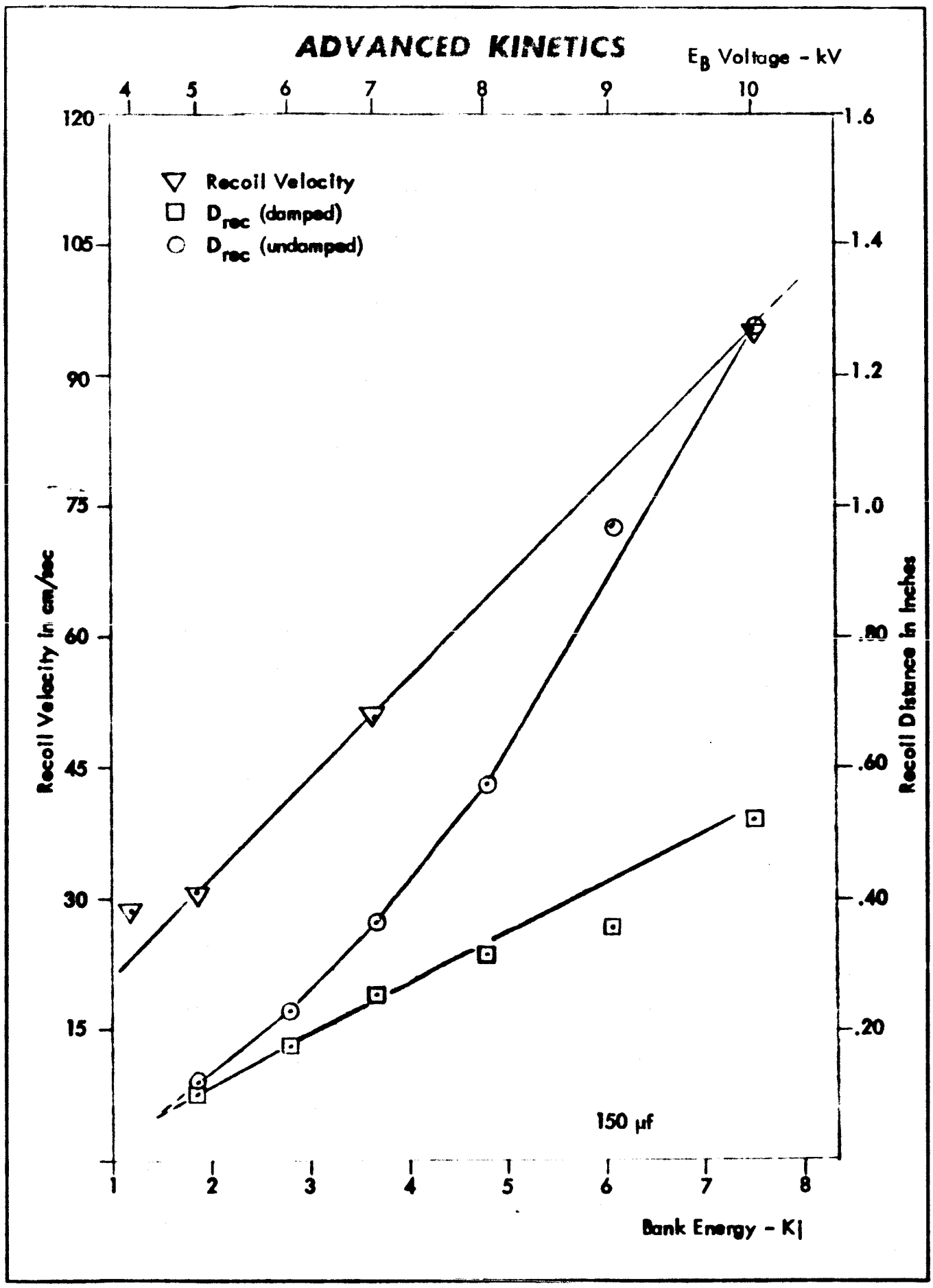

Fig. 21: Recoil Data for Hammer II

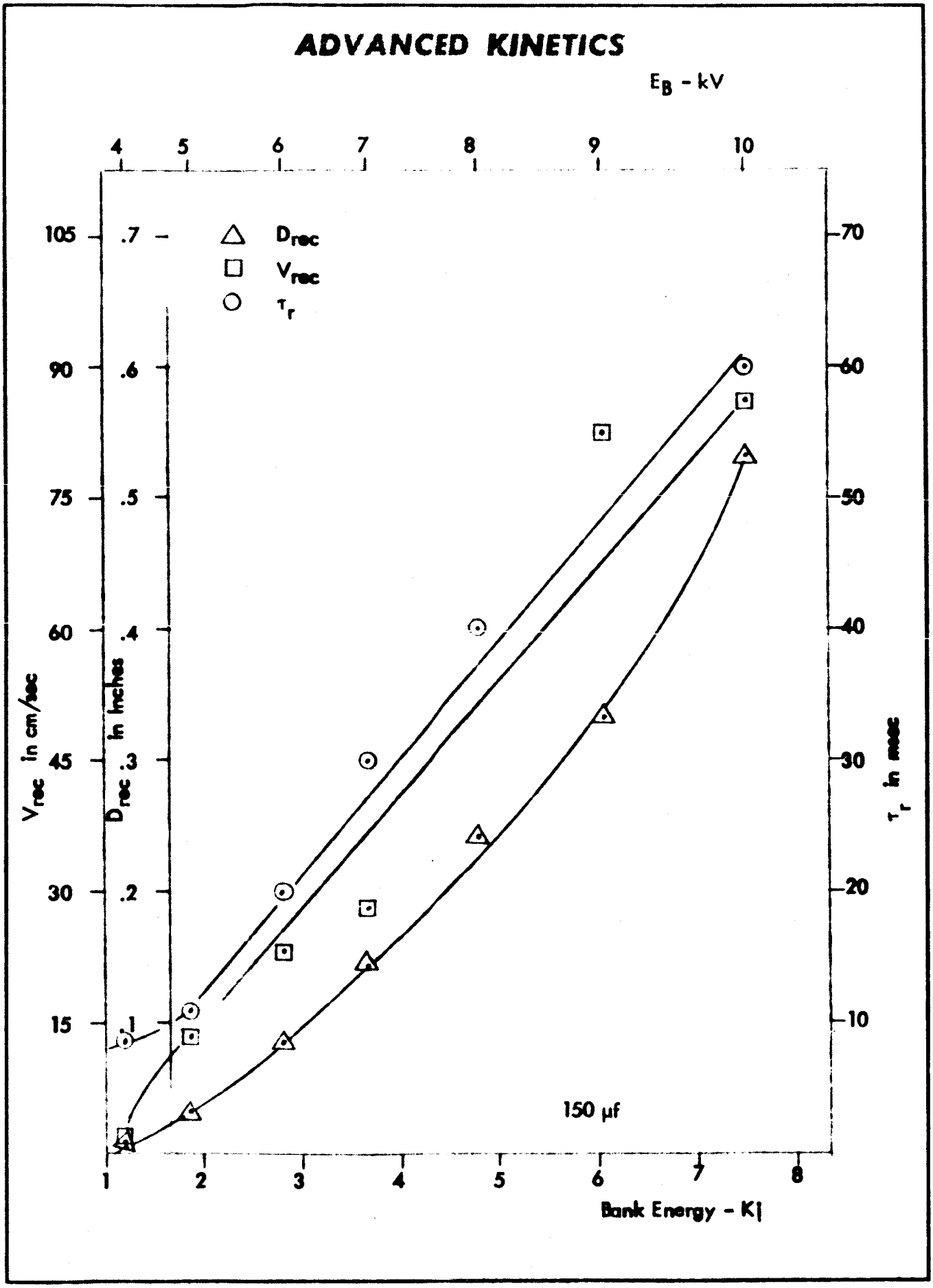

Fig. 22: Recoil Data for Hammer III

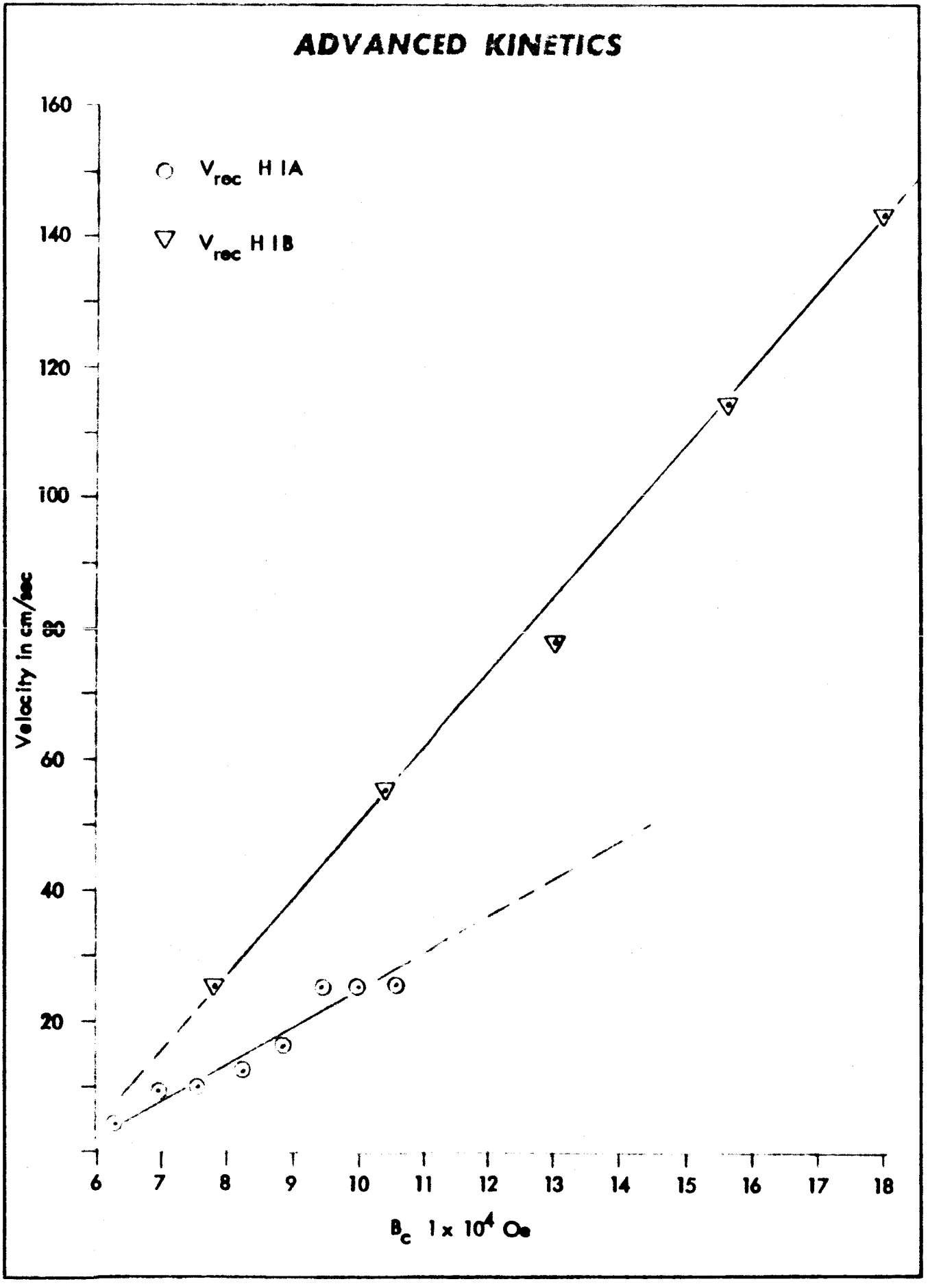

Fig. 23: Graphic Comparison of H IA and H IB Recoil Velocities vs Field